Journal of Computational Physics 229 (2010) 6534–6547

Contents lists available at ScienceDirect

Journal of Computational Physics

journal homepage: www.elsevier.com/locate/jcp

# A linear nonconforming finite element method for Maxwell's equations in two dimensions. Part I: Frequency domain

Peter Hansbo [a], Thomas Rylander [b,*]

[a] Department of Mathematical Sciences, Chalmers University of Technology and University of Gothenburg, SE-41296 Göteborg, Sweden
[b] Department of Signals and Systems, Chalmers University of Technology, SE-41296 Göteborg, Sweden

ARTICLE INFO

*Article history:*
Received 28 June 2009
Received in revised form 18 March 2010
Accepted 16 May 2010
Available online 26 May 2010

*Keywords:*
Maxwell's equations
Stabilized methods
Finite element
Interior penalty method
Nonconforming method

ABSTRACT

We suggest a linear nonconforming triangular element for Maxwell's equations and test it in the context of the vector Helmholtz equation. The element uses discontinuous normal fields and tangential fields with continuity at the midpoint of the element sides, an approximation related to the Crouzeix–Raviart element for Stokes. The element is stabilized using the jump of the tangential fields, giving us a free parameter to decide. We give dispersion relations for different stability parameters and give some numerical examples, where the results converge quadratically with the mesh size for problems with smooth boundaries. The proposed element is free from spurious solutions and, for cavity eigenvalue problems, the eigenfrequencies that correspond to well-resolved eigenmodes are reproduced with the correct multiplicity.



## 1. Introduction

The electric field solution to Maxwell's equations resides in $H(\mathrm{curl})$ and it requires tangential continuity. Imposing $H^1$-continuity on the approximation of the electric field usually leads to pollution of the spectrum, i.e. unphysical non-zero eigenvalues that mix with the lowest physical eigenvalues. In such a situation, modes that should have zero eigenvalues (corresponding to gradient fields) in the continuous setting have non-zero eigenvalues in the discrete setting. This has led to the introduction of vector elements [1,2] that are tailor-made for approximation in $H(\mathrm{curl})$ and they have become very popular for numerical simulations in electromagnetics, cf. Monk [3]. For such elements of the lowest order, the degrees of freedom are associated with the edges of the element and therefore they are often referred to as edge elements.

The triangular edge elements suffer in that the corresponding mass matrix cannot be lumped (with positive entries in the mass matrix) unless an angle condition is fulfilled [4], or other non-standard measures are taken [5,6]. In general, the standard edge elements thus require implicit time-stepping. On the other hand, curl-conforming approximations on rectangles and bricks do allow for mass-lumping and explicit time-stepping, cf. Cohen [7]. For example, the lowest order curl-conforming approximation on rectangles and bricks can be lumped by means of trapezoidal integration, and its analogue finite difference scheme was introduced by Yee [8]. Thus, it is often referred to as the Yee scheme but it is probably more well-known as the finite-difference time-domain (FDTD) scheme [9], which emphasizes its typical usage for electrodynamic problems. For the purpose of boundary modelling, the Yee scheme has to be coupled to other methods. It is feasible to couple implicitly time-stepped tetrahedrons (or triangles) with the Yee scheme in time-domain methods, cf. Degerfeldt and Rylander [10]. For the purpose of explicit schemes on unstructured meshes, discontinuous Galerkin (DG) methods can be formulated on simplicial meshes [11]. These have been explored in the setting of time-harmonic problems [12] and eigenvalue problems

* Corresponding author. Tel.: +46 (0)31 7721735; fax: +46 (0)31 7721748.
*E-mail address:* rylander@chalmers.se (T. Rylander).

0021-9991/$ - see front matter © 2010 Published by Elsevier Inc.
doi:10.1016/j.jcp.2010.05.009

[13]. They do allow for mass-lumping and explicit time-stepping on unstructured simplicial meshes, cf. Hesthaven and Warburton [14]; however, DG methods achieve mass-lumping at the cost of extra degrees of freedom at the inter-element boundaries – a solution that becomes particularly expensive for the low-order approximations that are popular for engineering applications.

In this paper, we propose a new nonconforming element for the approximation of the curl-conforming electric field of Maxwell's equations in two dimensions. Our element yields a diagonal mass matrix and thus explicit time-stepping can be used on arbitrary unstructured meshes. The element represents linear field variations exactly and it has degrees of freedom associated with the edges of the element, where the tangential field component is continuous at the midpoint of each edge and the normal field component is discontinuous. Consequently, we achieve a significant reduction in the number of degrees of freedom as compared to the corresponding DG method without sacrificing the ability to perform explicit time-stepping. We demonstrate that our new element yields very accurate approximations on a grid of equilateral triangles. In particular, we use this type of discretization in the homogeneous bulk of the computational domain, and revert to an unstructured mesh of body-conforming triangles in the vicinity of curved boundaries.

In this article, we focus on the characteristic features of our new element for frequency-domain problems. Time-domain formulations that exploit the proposed element are postponed to a companion article. Our element contains the linear curl-conforming element [2] as a special case and, consequently, it is feasible for us to exploit techniques developed for linear curl-conforming elements. For example, the so-called perfectly matched layer [15] is popular for unbounded problems and there are finite element formulations in both frequency domain [16] and time domain [17]. Our proposed element is also a good candidate for coupling the Yee scheme on rectangles to a boundary-fitted triangular mesh, where the Yee scheme is represented by rectangular lowest-order edge elements with mass-lumping [18] and Nitsche's method is applied at the interface [10].

## 2. Problem formulation and finite element method

We consider Maxwell's double curl eigenvalue problem in two somewhat different situations: (i) plane wave propagation in free space for a given wave number $\boldsymbol{k}$ which gives the numerical dispersion relation $\omega(\boldsymbol{k})$ of the proposed element; and (ii) a cavity resonator that is defined by the bounded domain $\Omega$ with perfect electrically conducting boundary $\partial\Omega$ and outward pointing normal $\boldsymbol{n}$. Thus, we wish to find the electric field $\boldsymbol{E}$ and frequency $\omega$ such that

$$\nabla\times\nabla\times\boldsymbol{E}-\left(\frac{\omega}{c_0}\right)^2\boldsymbol{E}=0\quad\text{in }\Omega, \tag{1}$$

with (i) $\Omega=\mathbb{R}^2$ for the dispersion analysis and (ii) a bounded domain $\Omega$ with $\boldsymbol{n}\times\boldsymbol{E}=0$ on $\partial\Omega$ for the cavity resonator problem. Here, $c_0$ denotes the speed of light in vacuum.

For the presentation of the new element, we focus on the cavity resonator problem and postpone further discussions on the dispersion analysis to Section 4. For the cavity resonator problem stated in weak form, we seek

$$\boldsymbol{E}\in V:=\{\boldsymbol{v}\in H(\mathrm{curl};\Omega):\boldsymbol{v}\times\boldsymbol{n}=0\text{ on }\partial\Omega\}$$

such that

$$\int_\Omega(\nabla\times\boldsymbol{E})(\nabla\times\boldsymbol{v})d\Omega-\left(\frac{\omega}{c_0}\right)^2\int_\Omega\boldsymbol{E}\cdot\boldsymbol{v}d\Omega=0 \tag{2}$$

for all $\boldsymbol{v}\in V$. Here

$$H(\mathrm{curl};\Omega):=\{\boldsymbol{v}:\boldsymbol{v}\in L_2(\Omega)\text{ and }\nabla\times\boldsymbol{v}\in L_2(\Omega)\}.$$

In order to discretize this problem, we let $\mathcal{T}_h$ denote a triangulation of $\Omega$ into simplices $T$ of diameter $h_T$, and let $\mathcal{E}_h$ denote the set of edges $e$, of length $h_e$, in $\mathcal{T}_h$. We then define the following nonconforming finite element space:

$$V_h:=\Big\{\boldsymbol{v}\in[L_2(\Omega)]^2:\boldsymbol{v}\in[P^1(T)]^2\forall T\in\mathcal{T}_h,\ \boldsymbol{n}\times\boldsymbol{v}\text{ is continuous at the midpoints of all interior edges,}\\ \text{and }\boldsymbol{n}\times\boldsymbol{v}=0\text{ at the midpoints of all edges along }\partial\Omega\}.$$

We note that this space is related to the classical Crouzeix–Raviart (CR) space [19], but with edge midpoint continuity enforced only for the tangential component. The standard CR element is known not to converge for the Maxwell double curl problem, cf. Brenner et al. [20] (where instead an element-wise divergence free version of the CR element was analyzed and shown to converge; related results are given in [21] and, in particular addressing the eigenproblem, in [22]).

Fig. 1 shows the degrees of freedom for the proposed finite element. The direction of the vector field for each basis function is constant inside the element. Further, each basis function is of unity magnitude at the edge midpoint associated with the degree of freedom and zero at the other two other edge midpoints. We express the CR basis functions as

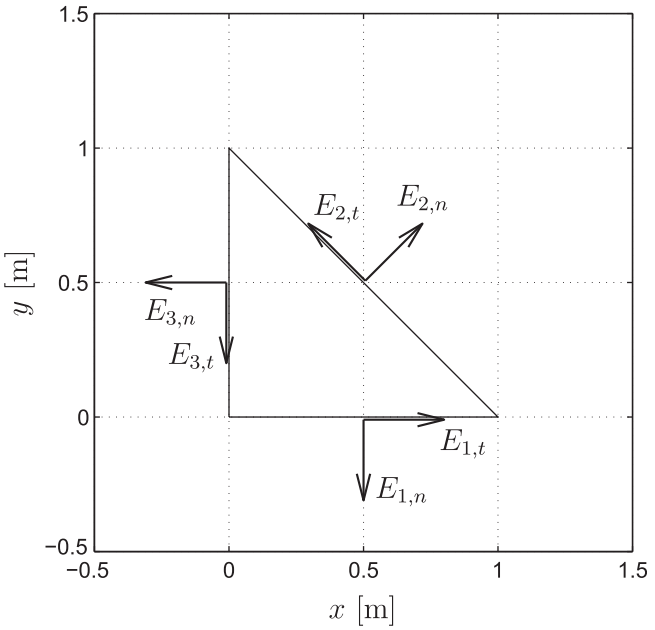


**Fig. 1.** The degrees of freedom for the proposed finite element.

$$\varphi_1 = 1 - 2y$$
$$\varphi_2 = 2(x + y) - 1$$
$$\varphi_3 = 1 - 2x$$

on the unit triangle. Thus, the basis functions associated with the degrees of freedom $E_{i,n}$ are given by $\boldsymbol{n}_i\varphi_i$ for $i = 1$, 2 and 3, where $\boldsymbol{n}_i$ denotes the unit normal to the $i$th edge of the unit triangle. The corresponding basis functions associated with $E_{i,t}$ are given by $\boldsymbol{z} \times \boldsymbol{n}_i\ \varphi_i$ for $i = 1$, 2 and 3, where $\boldsymbol{z}$ is the unit normal to the plane of the unit triangle.

Denoting the jump of the tangential component of $\boldsymbol{v} \in V_h$ across edges by $[\![\boldsymbol{n} \times \boldsymbol{v}]\!]$, with $[\![\boldsymbol{n} \times \boldsymbol{v}]\!] = \boldsymbol{n} \times \boldsymbol{v}$ if the edge is on $\partial\Omega$, where $\boldsymbol{n}$ is a normal to the edge $e$, our finite element method is to find $(\boldsymbol{E}^h, \omega^2) \in V_h \times \mathbb{R}$ such that

$$a_h(\boldsymbol{E}^h, \boldsymbol{v}) - \left(\frac{\omega}{c_0}\right)^2 (\boldsymbol{E}^h, \boldsymbol{v}) = 0 \quad \forall \boldsymbol{v} \in V_h, \tag{3}$$

where

$$a_h(\boldsymbol{u}, \boldsymbol{v}) := \int_\Omega (\nabla_h \times \boldsymbol{u})(\nabla_h \times \boldsymbol{v}) d\Omega + \sum_{e \in \mathcal{E}_h} \int_e \frac{\gamma}{h_e} [\![\boldsymbol{n} \times \boldsymbol{u}]\!][\![\boldsymbol{n} \times \boldsymbol{v}]\!] ds \tag{4}$$

and

$$(\boldsymbol{u}, \boldsymbol{v}) := \int_\Omega \boldsymbol{u} \cdot \boldsymbol{v} d\Omega.$$

Here, $\nabla_h\times$ denotes the element-wise application of the curl operator and $\gamma$ is a user specified penalty parameter. We note that the tangential jumps have been added to the equation in the same manner as in a DG method in order to increase stability of our numerical scheme. Computational experience shows that this term (with $\gamma > 0$) is indeed necessary; the piecewise $H(\mathrm{curl}; \Omega)$-norm is too weak to control the jumps (cf. also [23]). We also note that the DG scheme has two additional terms compared to (3); the bilinear form for DG can be written

$$a_h^{\mathrm{DG}}(\boldsymbol{u}, \boldsymbol{v}) = a_h(\boldsymbol{u}, \boldsymbol{v}) - \sum_{e \in \mathcal{E}_h} \int_e ([\![\boldsymbol{n} \times \boldsymbol{u}]\!]\{\nabla_h \times \boldsymbol{v}\} + [\![\boldsymbol{n} \times \boldsymbol{v}]\!]\{\nabla_h \times \boldsymbol{u}\}) ds,$$

where $\{\cdot\}$ denotes a mean value of the indicated quantity across the edge $e$. These are consistency terms necessary to retain Galerkin orthogonality, yielding a best approximation result underlying optimal convergence properties. For our approximation, these terms are zero since $\nabla_h \times \boldsymbol{v}$ is piecewise constant and the mean value of $[\![\boldsymbol{n} \times \boldsymbol{v}]\!]$ is zero for all $\boldsymbol{v} \in V_h$. Thus our method is (weakly) consistent in the same sense as a standard DG method (the idea of retaining the stabilization terms for Crouzeix–Raviart was first used in another context in [24]).

In the theoretical framework for the analysis of DG approximations of the Maxwell eigenproblem presented by Buffa and Perugia [25], a key ingredient in the analysis is the use of an interpolant onto the corresponding edge element space. Due to the large size of the DG basis, the edge elements constitute a subset thereof, a fact that can be used in the analysis. One may view our method as a way of reducing the number of unknowns in the DG method without losing the property that the edge element basis is a subset of $V_h$: the linear edge element has full tangential continuity and a complete linear approximation inside the elements, cf. [2]. This space, with two degrees of freedom per edge, constitutes a subset of $V_h$ with its three degrees of freedom per (interior) edge (a subset obtained as $\gamma \to \infty$). Note that this is not the case for the standard Crouzeix–Raviart basis with its additional mean normal continuity.

The null space of our element is identical to that of the linear edge element in the limit $\gamma \to \infty$. For finite values of $\gamma$, the proposed element allows the tangential component of the vector field to be discontinuous except at the midpoint of each edge in the mesh, which clearly yields a larger space than that of the linear edge element. Our formulation requires that modes that belong to the null space of the bilinear form (4) with $\gamma > 0$ satisfy two conditions: (i) element-wise application of the curl operator is zero; and (ii) tangential continuity at element boundaries. The gradient fields of the linear edge element clearly satisfy these two requirements and, consequently, they are part of the null space of the bilinear form (4) for finite values of $\gamma$. Numerical tests with $\gamma > 0$ demonstrate that the dimension of the null space is identical to that of the linear edge element. Thus, we conclude that the proposed element and the linear edge element have identical null spaces when $\gamma > 0$.

Some advantages of our approach compared to the linear edge element are:

- Mass-lumping is inherent. Expressed on the unit triangle shown in Fig. 1, we exploit the quadrature rule

$$\int_{S_{\text{unit triangle}}} f(x,y)d\Omega \simeq \frac{1}{6}\left[f\left(\frac{1}{2},0\right)+f\left(\frac{1}{2},\frac{1}{2}\right)+f\left(0,\frac{1}{2}\right)\right]$$

that integrates quadratic polynomials exactly and yields a diagonal mass matrix for the proposed element.

- We have only one tangential degree of freedom per edge, which fits well with Yee's finite difference method.

Finally, we remark that an alternative implementation of the element would be to follow Burman and Hansbo [26] and replace

$$\int_e \frac{\gamma}{h_e}[\![\boldsymbol{n}\times\boldsymbol{u}]\!][\![\boldsymbol{n}\times\boldsymbol{v}]\!]ds$$

by

$$\int_e \gamma^* h_e[\![\boldsymbol{t}\cdot(\boldsymbol{t}\cdot\nabla\boldsymbol{u})]\!][\![\boldsymbol{t}\cdot(\boldsymbol{t}\cdot\nabla\boldsymbol{v})]\!]ds$$

where $\boldsymbol{t}$ is a unit vector tangential to the edge and $\gamma^* > 0$ is a stabilization parameter (different from $\gamma$). This gives the same stability (cf. Lemma 9 in [26] for the basic argument) but requires only one Gauss-point per edge to integrate exactly.

## 3. A brief discussion on the theoretical aspects of the method

In [25] a general framework for the analysis of DG methods was presented; there it was established that two basic properties constitute necessary and sufficient conditions for a DG method to be free of spurious solutions. In order to define these properties, we first define the sum space $V(h) = V + V_h$, and introduce the seminorm and norm (defined on both $V_h$ and $V(h)$)

$$|\boldsymbol{v}|^2_{V(h)} = \|\nabla_h\times\boldsymbol{v}\|^2_{L_2(\Omega)} + \sum_{e\in\mathcal{E}_h}\int_e \frac{1}{h_e}|[\![\boldsymbol{n}\times\boldsymbol{v}]\!]|^2 ds,$$
$$\|\boldsymbol{v}\|^2_{V(h)} = |\boldsymbol{v}|^2_{V(h)} + \|k\boldsymbol{v}\|^2_{L_2(\Omega)}.$$

where $k = \omega/c_0$. We also define the kernel of $a_h(\cdot,\cdot)$ and its orthogonal complement by

$$K_h := \{\boldsymbol{v}\in V_h : a_h(\boldsymbol{v},\boldsymbol{w}) = 0 \quad \forall \boldsymbol{w}\in V_h\},$$
$$K_h^\perp := \{\boldsymbol{v}\in V_h : (\boldsymbol{v},\boldsymbol{w})_{V(h)} = 0 \quad \forall \boldsymbol{w}\in K_h\};$$

where $(\cdot,\cdot)_{V(h)}$ is the scalar product corresponding to the norm $\|\cdot\|_{V(h)}$.

The necessary and sufficient properties of [25] can now be stated as follows.

1. A discrete Friedrich's inequality: there exists $C > 0$ independent of the mesh size such that

$$\|k\boldsymbol{v}\|^2_{L_2(\Omega)} \leqslant C\mathrm{Re}[a_h(\boldsymbol{v},\boldsymbol{v})] \quad \forall \boldsymbol{v}\in K_h^\perp$$

2. A gap property: for $h$ small enough, there exists, for any given $\boldsymbol{w}_h \in K_h^\perp$,

$$\boldsymbol{w} \in H(\mathrm{div}_k^0;\Omega) := \{\boldsymbol{v} \in [L_2(\Omega)]^2 : \nabla\cdot(k\boldsymbol{v}) = 0\},$$

such that

$$\|\boldsymbol{w}-\boldsymbol{w}_h\|_{L_2(\Omega)} \leqslant \eta_h \|\boldsymbol{w}_h\|_{V(h)} \quad \text{with } \eta_h \to 0 \text{ as } h \to 0. \tag{5}$$

The crucial point in the proof of these properties is the use of the Nédélec space $V_h^c = V_h \cap V$ consisting of the second family (of degree 1 in our case), see [2]; more precisely the use of an operator $\Pi_h^c : V_h \to V_h^c$ such that

$$\begin{aligned} \|\boldsymbol{v}-\Pi_h^c\boldsymbol{v}\|_{L_2(\Omega)}^2 &\leqslant C\sum_{e\in\mathcal{E}_h}\int_e h_e|[\![\boldsymbol{n}\times\boldsymbol{v}]\!]|^2 ds,\\ \|\boldsymbol{v}-\Pi_h^c\boldsymbol{v}\|_{V(h)}^2 &\leqslant C\sum_{e\in\mathcal{E}_h}\int_e \frac{1}{h_e}|[\![\boldsymbol{n}\times\boldsymbol{v}]\!]|^2 ds. \end{aligned} \tag{6}$$

The existence of an operator with these properties implies that there is a curl-conforming finite element function close to any function in $V_h$, and that we can decompose $\boldsymbol{v} \in V_h$ as $\boldsymbol{v} = \boldsymbol{v}^c + \boldsymbol{v}^\perp$, where $\boldsymbol{v}^c \in V_h^c$ and $\boldsymbol{v}^\perp = (1-\Pi_h^c)\boldsymbol{v}$, where $\boldsymbol{v}^\perp$ is under control due to (6), see [25] for details.

Now, the existence of the operator $\Pi_h^c$ hinges on (a) the discontinuous space containing the Nédélec space of the same polynomial order, and (b) an additional bound on the tangential jumps in the approximation, cf. [27, Appendix, Steps 4–5]. We have already addressed (a) above. As for (b), the pertinent bound on the tangential jumps holds *a fortiori* on the Crouzeix–Raviart space because of the mean continuity property, and we conclude that the theory developed in [25] for fully discontinuous Galerkin methods (of arbitrary order) carries over to our case.

## 4. Numerical tests

We test the proposed element on three different problems: (i) dispersion analysis based on plane wave propagation in free space; (ii) a cavity resonator problem with regular field solutions; and (iii) a cavity resonator problem that features a sharp corner which supports field singularities. In the following, we evaluate the stabilization term in the bilinear form (4) by means of trapezoidal integration.

### 4.1. Dispersion analysis

We use a plane wave on the form $\boldsymbol{E} = \boldsymbol{E}_0\exp[i(\omega t - \boldsymbol{k}\cdot\boldsymbol{r})]$ to compute the numerical dispersion relation on a periodic grid. The periodic grid exploits a rhombic unit cell that is repeated in order to discretize $\mathbb{R}^2$. The unit cell is divided into two triangles, which makes it feasible to formulate an eigenvalue problem with nine degrees of freedom given the proposed element. Fig. 2 shows part of the discretization with the global degrees of freedom: (i) black arrows – the nine independent

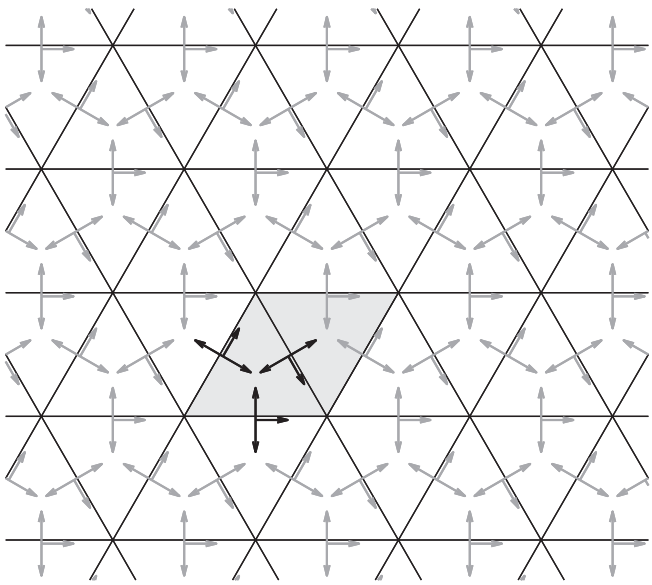

**Fig. 2.** Part of the periodic grid of equilateral triangles with the global degrees of freedom: (i) black arrows – the nine independent degrees of freedom associated with the unit cell shown by the gray rhomb; and (ii) gray arrows – dependent degrees of freedom.

degrees of freedom associated with the unit cell shown by the gray rhomb; and (ii) gray arrows – dependent degrees of freedom. A dependent degree of freedom (located at $\boldsymbol{r}_\mathrm{d}$) can be represented by means of a phase shift $\exp[-i\boldsymbol{k}\cdot\Delta\boldsymbol{r}]$ multiplied by the corresponding independent degree of freedom (located at $\boldsymbol{r}_\mathrm{i}$) in the unit cell, where $\Delta\boldsymbol{r} = \boldsymbol{r}_\mathrm{d} - \boldsymbol{r}_\mathrm{i}$. We solve the eigenvalue problem in terms of its eigenmodes and the corresponding eigenvalues $\omega^2$, where the frequency $\omega$ is a function of a prescribed wavevector $\boldsymbol{k}$. The analytically computed dispersion relation yields three possible solutions: $\omega = c_0 k$; $\omega = 0$; and $\omega = -c_0 k$ (here, $\omega = 0$ is associated with an electric field that can be expressed as the gradient of a scalar potential and $\omega = -c_0 k$ is discarded since it yields a wave that propagates in the direction opposite to $\boldsymbol{k}$).

#### 4.1.1. Choice of the stabilization parameter

Let $\|\cdot\|_{k_\mathrm{max}}$ denote the $L_1$-norm evaluated on the disc shaped region $k \leqslant k_\mathrm{max}$. Fig. 3 shows the relative error $\|\omega_\mathrm{n} - \omega_\mathrm{a}\|_{k_\mathrm{max}} / \|\omega_\mathrm{a}\|_{k_\mathrm{max}}$ as a function of the parameter $\gamma$ for a grid of equilateral triangles characterized by the edge length $h_e$: (i) $h_e k_\mathrm{max}/\pi = 0.3$ – dashed curve with the minimum at $\gamma = 1.17$; (ii) $h_e k_\mathrm{max}/\pi = 0.5$ – solid curve with the minimum at $\gamma = 1.19$; and (iii) $h_e k_\mathrm{max}/\pi = 0.7$ – dash-dotted curve with the minimum at $\gamma = 1.22$. Here, $\omega_\mathrm{a}$ is the analytical frequency and $\omega_\mathrm{n}$ is the corresponding numerical value (in addition, we performed the same type of parameter study in the $L_\infty$-norm and the optimized values for the stabilization parameter deviate about 1% or less from the values obtained with the $L_1$-norm).

Fig. 4 shows the pointwise relative error $|\omega_\mathrm{n} - \omega_\mathrm{a}|/|\omega_\mathrm{a}|$ as a function of the wavevector $\boldsymbol{k}$, given the optimized $\gamma = \gamma_\mathrm{opt} = 1.19$ for the region $h_e k/\pi \leqslant 0.5$. It is clear that the relative error in the frequency is very low for a large region in $\boldsymbol{k}$-space. We also note that the relative error in the dispersion relation is proportional to $(h_e k)^2$ in the domain of asymptotic convergence, which is confined to the region $h_e k/\pi \lessapprox 0.2$. Given this result, we find it useful to exploit a structured grid of equilateral triangles in homogeneous parts of the computational domain and other element shapes only in the vicinity of complicated boundaries, where we wish to have a body-conforming mesh or resolve rapid field variations due to sharp corners.

Fig. 5 shows the relative error $|\omega_\mathrm{n} - \omega_\mathrm{a}|/|\omega_\mathrm{a}|$ for a wave that propagates in the horizontal direction through the grid of equilateral triangles shown in Fig. 2. The relative error in Fig. 5 is shown for three different values of the stabilization parameter: $\gamma = 0.1\gamma_\mathrm{opt}$ – dashed curve; $\gamma = \gamma_\mathrm{opt}$ – solid curve; and $\gamma = 10\gamma_\mathrm{opt}$ – dash-dotted curve. We notice that it is feasible to reduce the relative error to very low levels for wavelengths that are rather poorly resolved by the cell size, should the parameter $\gamma$ be given an appropriate value for a grid of equilateral triangles.

#### 4.1.2. Characteristic features of the proposed element

In this section, we consider a plane wave that propagates in the horizontal direction in Fig. 2. Fig. 6 shows the analytical dispersion relation by the solid line together with the numerical dispersion relation for different choices of the stabilization parameter: $\gamma = 0.5\gamma_\mathrm{opt}$ – dotted curve; $\gamma = \gamma_\mathrm{opt}$ – dashed curve; and $\gamma = 2\gamma_\mathrm{opt}$ – dash-dotted curve. Here, $\gamma_\mathrm{opt} = 1.19$ and this choice is discussed in the previous section. For all wavenumbers, we note that the numerical frequency is too large for $\gamma = 2\gamma_\mathrm{opt}$ and too small for $\gamma = 0.5\gamma_\mathrm{opt}$. Also, we note that the numerical dispersion relation crosses the analytical dispersion relation for the choice $\gamma = \gamma_\mathrm{opt}$ at $h_e k/\pi \approx 0.42$.

The unit cell of the grid shown in Fig. 2 features nine independent degrees of freedom and, consequently, the discrete eigenvalue problem yields nine numerical frequencies for a given wave vector. Fig. 7 shows the analytical dispersion relation

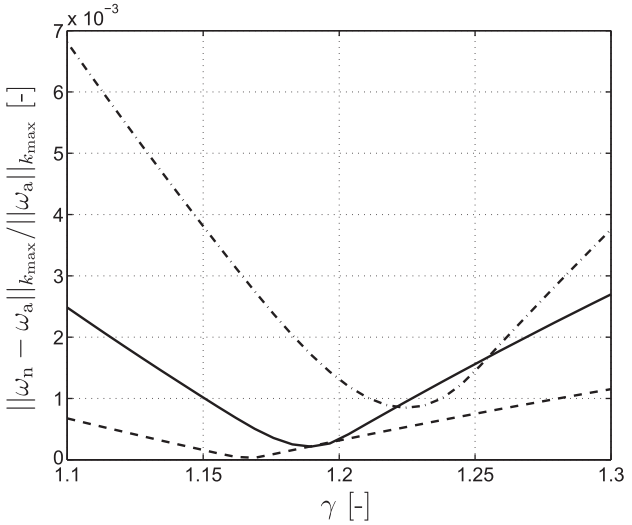


**Fig. 3.** The relative error $\|\omega_\mathrm{n} - \omega_\mathrm{a}\|_{k_\mathrm{max}} / \|\omega_\mathrm{a}\|_{k_\mathrm{max}}$ on the disc shaped region $k \leqslant k_\mathrm{max}$ as a function of the parameter $\gamma$ for a grid of equilateral triangles: $h_e k_\mathrm{max}/\pi = 0.3$ – dashed curve; $h_e k_\mathrm{max}/\pi = 0.5$ – solid curve; and $h_e k_\mathrm{max}/\pi = 0.7$ – dash-dotted curve.

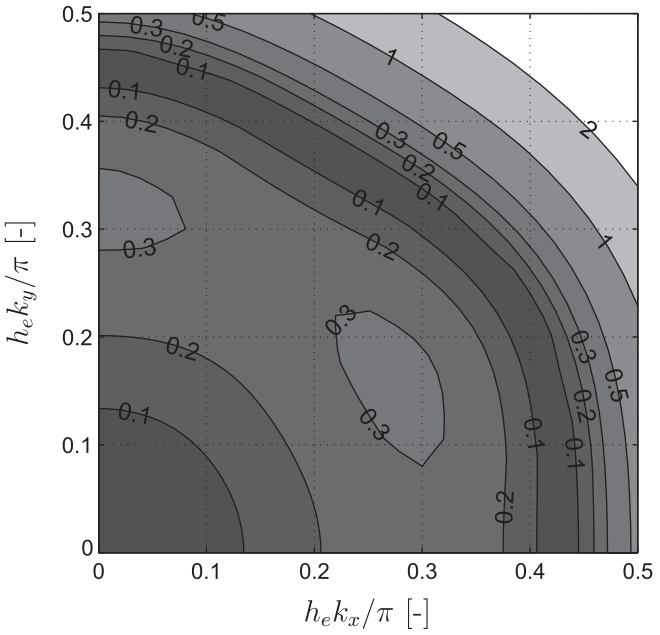


**Fig. 4.** The relative error $|\omega_n - \omega_a|/|\omega_a|$ in per mille as a function of $\boldsymbol{k}$ for a grid of equilateral triangles of edge length $h_e$ with $\gamma = 1.19$.

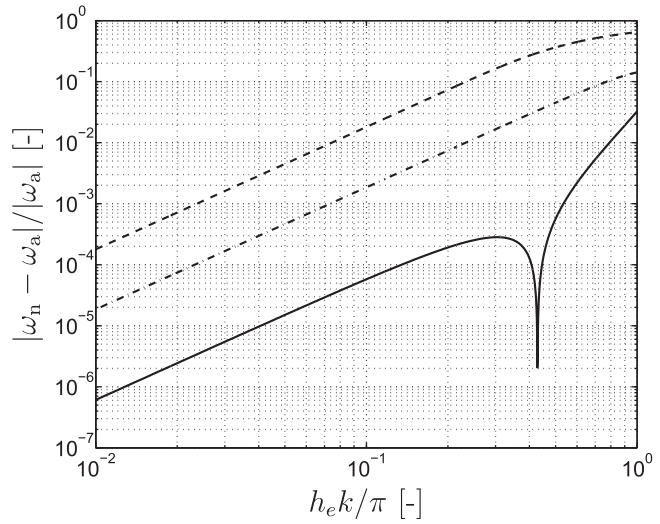


**Fig. 5.** The relative error $|\omega_n - \omega_a|/|\omega_a|$ on a grid of equilateral triangles for different values of the stabilization parameter: $\gamma = 0.1\gamma_{opt}$ – dashed curve; $\gamma = \gamma_{opt}$ – solid curve; and $\gamma = 10\gamma_{opt}$ – dash-dotted curve. The wave propagates along the horizontal axis in the grid shown in Fig. 2 and $\gamma_{opt} = 1.19$.

(by a solid curve) together with all the numerical frequencies (dashed curves) associated with the proposed element for $\gamma = \gamma_{opt}$ on a grid of equilateral triangles. This dispersion analysis confirms that the proposed element does not suffer from spurious modes, i.e. problems of the type that fields that vary on the scale of the grid yield frequencies in the same range as modes that are well-resolved by the grid, cf. Paulsen and Lynch [28] (we have performed this test for the full range of propagation directions and conclude that the influence on the results shown in Fig. 7 is insignificant). In the case of $\gamma > 0$, four of the branches (denoted `B1–B4`) correspond to conservative (gradient field) solutions with $\omega = 0$. One of these zero eigenvalues is associated with the node of the unit cell, where the continuous linear Lagrangian basis function $\phi_i$ has its degree of freedom. The remaining three zero eigenvalues are associated with edge-bubble basis functions that coincide with the three edges of the unit cell, where the potential is given by $\phi_i\phi_j$ and the indices $i$ and $j$ denote the end nodes of an edge in the unit cell. The lowest non-zero branch $\omega(\boldsymbol{k})$ (denoted `B5`) models the physical dispersion relation. The remaining four branches (denoted `B6–B9`) yield high numerical frequencies that do not mix with the physical dispersion relation `B5`, and therefore can easily be identified and disregarded (if the stabilization is removed by setting $\gamma = 0$, we have two zero eigenmodes associated with each edge of the unit cell, i.e. in total seven zero branches).

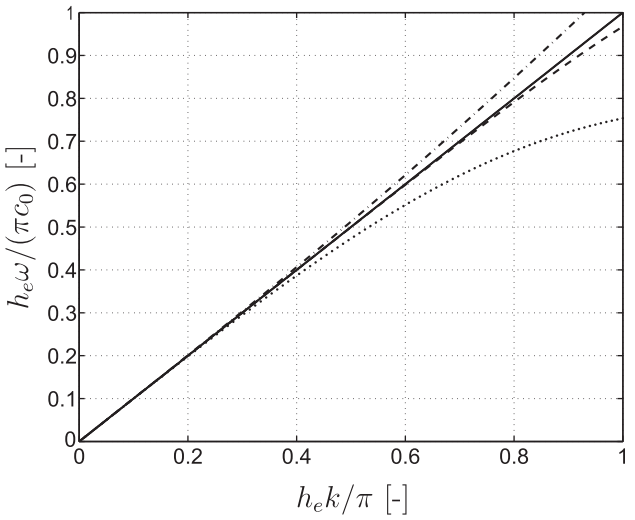


**Fig. 6.** Normalized numerical frequency as a function of the wavenumber on a grid of equilateral triangles for different values of the stabilization parameter: $\gamma = 0.5\gamma_{opt}$ – dotted curve; $\gamma = \gamma_{opt}$ – dashed curve; and $\gamma = 2\gamma_{opt}$ – dash-dotted curve. The wave propagates along the horizontal axis in the grid shown in Fig. 2, the analytical dispersion relation is shown by the solid curve and $\gamma_{opt} = 1.19$.

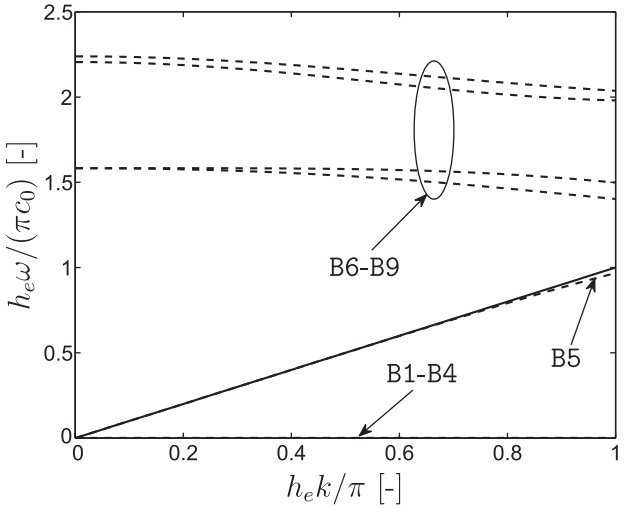


**Fig. 7.** Normalized numerical frequencies shown by dashed curves as a function of the wavenumber on a grid of equilateral triangles for $\gamma = \gamma_{opt} = 1.19$. The wave propagates along the horizontal axis in the grid shown in Fig. 2 and the analytical dispersion relation is shown by the solid curve.

### 4.2. Cavity analysis

Next, we consider the eigenvalue problem (1) on a bounded region $\Omega$ without holes, where we use the boundary condition $\boldsymbol{n} \times \boldsymbol{E} = 0$ on the boundary $\partial\Omega$. In all the tests that follow, the proposed element reproduces the lowest eigenvalues accurately with the correct multiplicity given that the corresponding eigenmodes are well-resolved. Moreover, the null space of the $\nabla \times \nabla \times$-operator is preserved. Let the number of internal nodes be denoted by $n_{in}$, the number of internal edges by $n_{ie}$ and the number of edges on the external boundary by $n_{be}$. We find that $\gamma = 0$ yields a null space of dimension $n_{in} + 2n_{ie} + n_{be}$. When stabilization is applied to all edges on the boundary of and internal to the computational domain, the dimension of the null space reduces to $n_{in} + n_{ie}$. This result is in agreement with our analysis of the null space associated with the $\nabla \times \nabla \times$-operator.

#### 4.2.1. Introductory example

As an example, we consider a square shaped cavity of side $L = \pi$ and Fig. 8 shows the two lowest eigenmodes computed by means of the proposed element. These eigenmodes are degenerated and their corresponding numerical eigenvalues are $k_1 = 1.000360$ and $k_2 = 1.000386$, which should be compared to the analytical degenerated eigenvalue $k_1 = k_2 = 1$. This

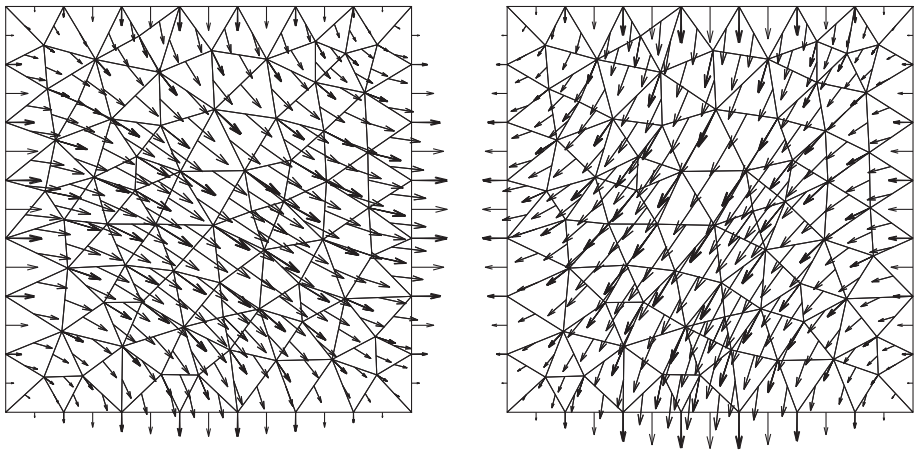

**Fig. 8.** The two lowest eigenmodes for a square shaped cavity. These eigenmodes are degenerated and this can be seen by rotating the right figure 90° in the counter clockwise direction.

demonstrates that the proposed element reproduces the lowest eigenvalues accurately with the correct multiplicity. Here, we emphasize that the corresponding eigenmodes are well-resolved by the mesh as shown by Fig. 8.

In addition, Fig. 9 shows the numerically computed spectrum of the 10 lowest eigenmodes for the mesh shown in Fig. 8. The analytical result is $(kL/\pi)^2 = n_x^2 + n_y^2$, where $n_x = 0,1,2,\ldots$ and $n_y = 0,1,2,\ldots$ with the combination $n_x = n_y = 0$ excluded. Thus, the 10 lowest eigenmodes sorted with respect to increasing eigenvalue $k^2$ have the mode indices $(n_x,n_y)$ equal to $(0,1)$, $(1,0)$, $(1,1)$, $(2,0)$, $(0,2)$, $(2,1)$, $(1,2)$, $(2,2)$, $(3,0)$ and $(0,3)$.

*4.2.2. Regular solution – grid with mainly equilateral triangles*

Here, we assess the performance of the proposed element, which appears to be most competitive on grids of equilateral triangles due to its low errors in the dispersion relation if an optimized value of $\gamma$ is used. Therefore, we use meshes of the type shown in Fig. 10. It consists of a structured grid of equilateral triangles in the homogeneous bulk of the computational domain in combination with a layer of unstructured triangles close to the boundary, which allows for a body-conforming discretization. Consequently, we cannot expect strictly uniform convergence for these meshes although we use uniform and hierarchic refinement for the equilateral triangles in the bulk. However, we note that the thickness of the layer of unstructured elements is proportional to mesh size and it is assumed that the unstructured body-fitted mesh yields a negligible contribution to the global error for sufficiently high resolutions. For homogeneous regions, we wish to emphasize that the main objective is to have a numerical scheme that accurately models the wave propagation. A grid of equilateral triangles is one possible choice for such a situation. In fact, it is easier and more efficient to work on such grids due to its repeatability

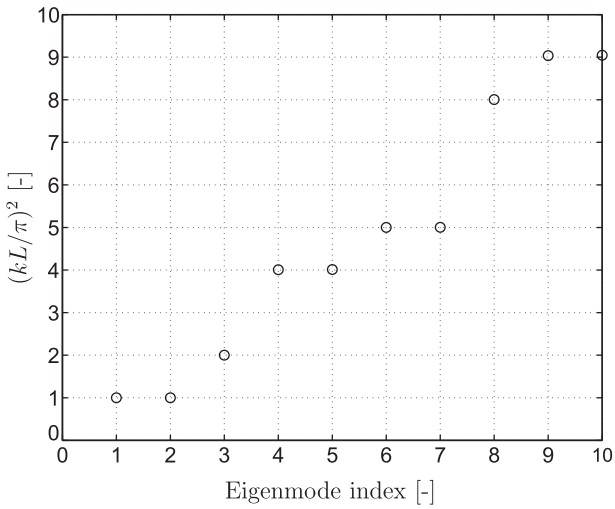


**Fig. 9.** Spectrum of eigenfrequencies $k^2$ plotted with respect to the eigenmode index for the 10 lowest eigenmodes.

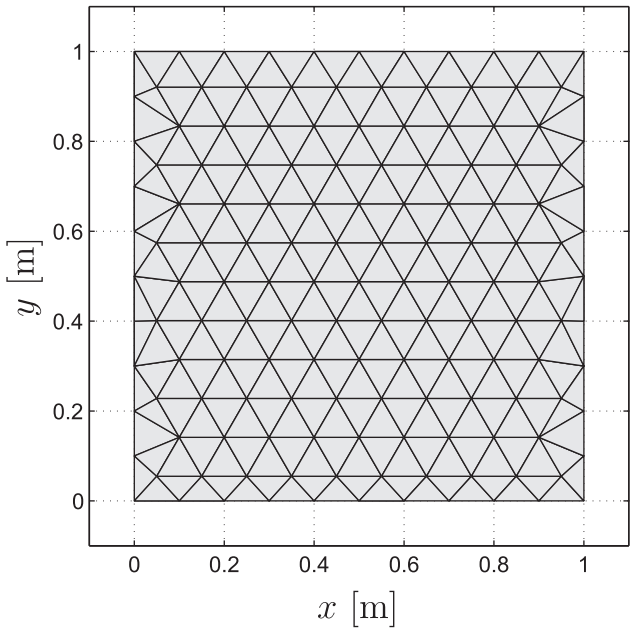


**Fig. 10.** Triangulation of square cavity that consists of two regions: (i) a structured grid of equilateral triangles in the homogeneous bulk of the computational domain; and (ii) an unstructured mesh of triangles that conform to the external boundary.

as compared to e.g. unstructured meshes. Consequently, we choose discretizations suitable for the proposed element and this type of discretization is shown in Fig. 10.

We compute the lowest eigenvalue for the square cavity and Fig. 11 shows its relative error for four different schemes: (◇) proposed element with $\gamma = 1.19$; (▽) incomplete linear edge element [1] on triangles; (△) complete linear edge element [2] on triangles; and (□) incomplete linear edge element [1] on squares with mass-lumping. Here, the solid lines show the results for a grid of mainly equilateral triangles as shown in Fig. 10 and the dashed line indicates the corresponding results for a structured grid of square elements. We note that the proposed element is significantly more accurate than both (i) the complete linear edge element on triangles and (ii) the lumped incomplete edge elements on squares. Furthermore, it displays an accuracy that is similar to the incomplete edge element on triangles. Monk [29] reported that the incomplete edge

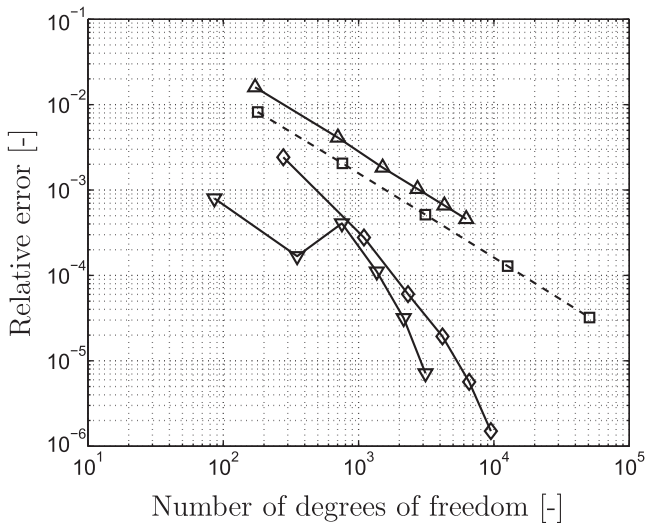


**Fig. 11.** Relative error of the lowest eigenvalue of a square cavity for four different schemes: (◇) proposed element with $\gamma = 1.19$; (▽) incomplete linear edge element on triangles; (△) complete linear edge element on triangles; and (□) incomplete linear edge element on squares with mass lumping. Here, solid lines are used for meshes with equilateral triangles in the homogeneous bulk of the computational domain and the dashed line show results for structured grid of squares.

element on a uniform grid of equilateral triangles yield a leading error term in the dispersion relation that is proportional to $h_e^4$, which supports the rapid order of convergence displayed in Fig. 11. We also verified that all the triangular elements yield a leading error term that is proportional to $h_e^2$ for hierarchically refined meshes of unstructured triangles. For comparative studies that involve incomplete and complete edge elements, we refer the reader to Refs. [30,31].

*4.2.3. Regular solution – unstructured mesh of triangles*

Next, we compute the maximum relative error

$$\delta_{\max} = \max_{m=1,\ldots,10} |\delta_m|$$

for the 10 lowest eigenmodes, where $\delta_m$ denotes the relative error for the $m$th eigenmode. Here, we consider a square cavity of side $L$ and use the four unstructured meshes shown in Fig. 12. Fig. 13 shows $\delta_{\max}$ as a function of the stabilization parameter $\gamma$ for the proposed element: Mesh #1 – dotted curve; Mesh #2 – dash-dotted curve; Mesh #3 – dashed curve; and Mesh #4 – solid curve. It is clear that the maximum relative error is low if the stabilization parameter $\gamma$ is chosen to be slightly larger than unity, which agrees well with the dispersion analysis performed on an infinite grid of equilateral triangles.

In order to put these results into the context of edge elements on triangles, Table 1 shows the maximum relative error $\delta_{\max}$ for the same eigenvalue problem solved with (i) incomplete linear edge elements and (ii) complete linear edge elements (for comparative studies that involve incomplete and complete edge elements, we refer the reader to Refs. [30,31]). The mode indices $(n_x, n_y)$ and the corresponding values for $k^2$ for the 10 lowest eigenmodes are given in Section 4.2.1. For a square cavity of side $L$, we wish to direct the readers' attention to the fact that $1/2 \leqslant L/\lambda \leqslant 3/2$ for the 10 lowest eigenmodes, where $\lambda = 2\pi/k$ is the wavelength associated with the eigenmode. Consequently, the eigenmodes with $(kL/\pi)^2 = 9$ feature 1.5 wavelengths along the side of the cavity and, for example, this gives less than 3 cells per wavelength for Mesh #1, which normally yields a very large error for a method based on linear elements and this is indeed the case for the incomplete and complete linear edge elements. Despite the very coarse resolution of the eigenmodes with $(kL/\pi)^2 = 9$, the new element proposed in this article yields a small $\delta_{\max}$ for good choices of the stabilization parameter. In fact, the proposed element shows a maximum relative error $\delta_{\max}$ that is smaller than the edge element results in Table 1 for substantial ranges of the stabilization parameter: (i) $0.86 < \gamma < 4.6$ for Mesh #1; (ii) $0.64 < \gamma < 100$ for Mesh #2; (iii) $0.80 < \gamma < 33$ for Mesh #3; and (iv) $0.64 < \gamma < 2.9$ for Mesh #4. In particular, it should be clear at this point that all the choices of the stabilization parameter $\gamma_{\text{opt}} = 1.17$, 1.19 and 1.22 presented in Section 4.1.1 are well within the intersection $0.86 < \gamma < 2.9$ of the four intervals associated with the four meshes considered here. We conclude that our new element yields a lower error than the incomplete and complete

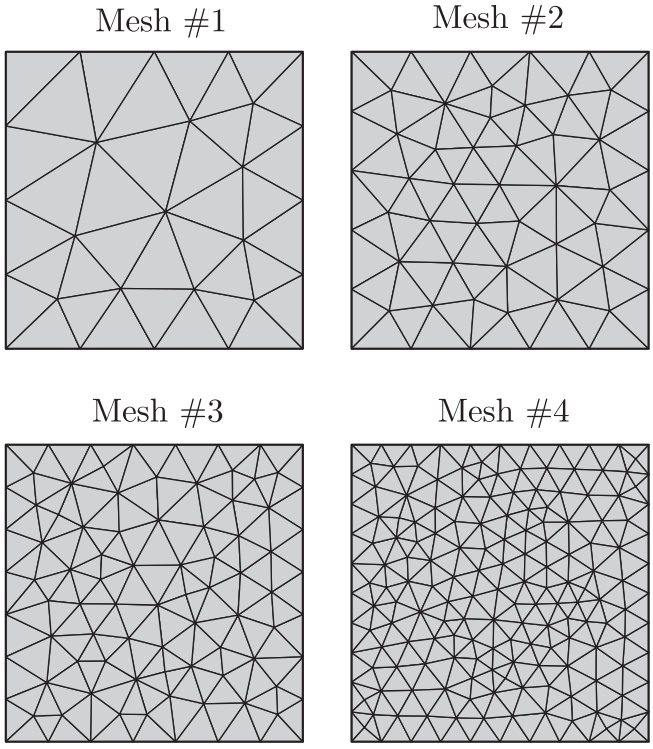


**Fig. 12.** Four unstructured meshes characterized by the circumradius $R$: $0.121 < R < 0.189$ – mesh #1; $0.070 < R < 0.116$ – mesh #2; $0.055 < R < 0.097$ – mesh #3; and $0.035 < R < 0.065$ – mesh #4.

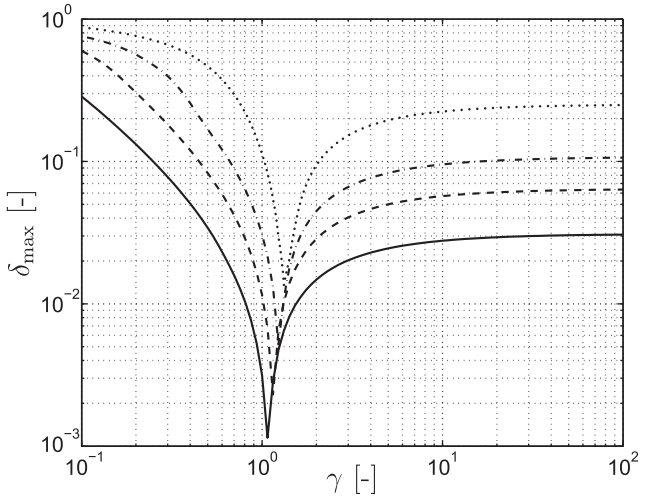


**Fig. 13.** Maximum relative error for the 10 lowest eigenvalues of a square cavity as a function of the stabilization parameter $\gamma$: mesh #1 – dotted curve; mesh #2 – dash-dotted curve; mesh #3 – dashed curve; and mesh #4 – solid curve.

**Table 1**
Maximum relative error $\delta_{\max}$ for the 10 lowest eigenvalues of a square cavity computed by (i) incomplete linear edge elements and (ii) complete linear edge elements.

| Discretization | $\delta_{\max}$ (–) | |
|---|---|---|
| | Incomplete | Complete |
| Mesh #1 | 0.19 | 2.27 |
| Mesh #2 | 0.11 | 0.97 |
| Mesh #3 | 0.03 | 0.58 |
| Mesh #4 | 0.02 | 0.28 |

linear edge elements for reasonable choices of the stabilization parameter, when compared with respect to the mesh size. Clearly, our element requires more degrees of freedom as compared to the incomplete and complete edge elements, and this issue is discussed in previous sections of this article. For larger values of the stabilization parameter in the range $10 < \gamma < 100$, the proposed element yields a maximum relative error $\delta_{\max}$ that is comparable to the incomplete linear edge elements.

*4.2.4. Singular solution*

Finally, we test the proposed element on an eigenvalue problem that features a sharp corner that supports a field singularity. Fig. 14 shows the L-shaped computational domain, where we again use the boundary condition $\boldsymbol{n} \times \boldsymbol{E} = 0$. In particular, we emphasize that the proposed element does not show any signs of generating spurious modes despite the presence of a singularity, and that the multiplicity of the lowest eigenvalue is correct. Here, we use a reference solution with six accurate digits computed by means of adaptive mesh refinement for quadratic Lagrangian shape functions for the magnetic field aligned with $\boldsymbol{z}$, i.e. the corresponding scalar Helmholtz equation eigenvalue problem for the magnetic field.

Fig. 15 shows the relative error of the lowest eigenfrequency as a function of the number of degrees of freedom for a uniformly refined mesh of right-angled triangles: ($\diamondsuit$) proposed element with $\gamma = \gamma_{\text{opt}} = 1.19$ shown by the dashed line and $\gamma = 10\gamma_{\text{opt}}$ shown by the solid line; ($\triangledown$) incomplete linear edge element [1] on triangles; and ($\triangle$) complete linear edge element [2] on triangles. It is clear that the relative error scales as $N^{-2/3} \propto h^{4/3}$ in the asymptotic region of convergence. This is expected [32] for a PEC corner that subtends the angle $\alpha = \pi/2$, where the electric field in the vicinity of the corner scales as $r^{-1+\pi/(2\pi-\alpha)}$ with respect to the distance $r$ to the corner. For the lowest eigenmode, the main contribution to the error in the eigenvalue stems from the field singularity at the sharp corner and we notice that our element with $\gamma = \gamma_{\text{opt}}$ yields results that are considerably more accurate than the incomplete linear edge element, when compared in terms of the number of degrees of freedom. It is well-known that the field behavior close to sharp corners is modeled well by complete linear edge elements [31], which is confirmed by the results shown in Fig. 15. It is interesting to notice that for the element proposed in this article, we achieve results that are quite similar to the complete linear edge elements when we use a larger stabilization parameter $\gamma = 10\gamma_{\text{opt}}$. We attribute this to the ability of the proposed element to represent linear field variations exactly, which is useful in the immediate vicinity of the singularity. These results suggest that larger values for the stabilization parameter may be useful in the vicinity of singularities.

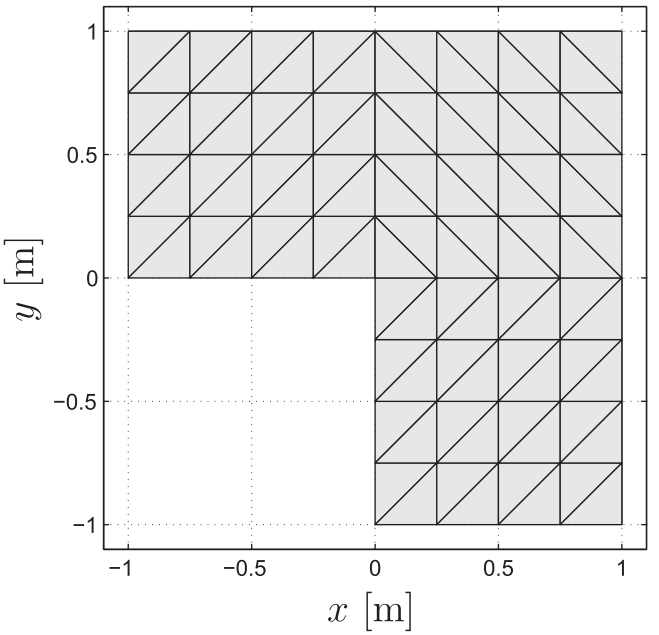


**Fig. 14.** Discretization of the L-shaped domain.

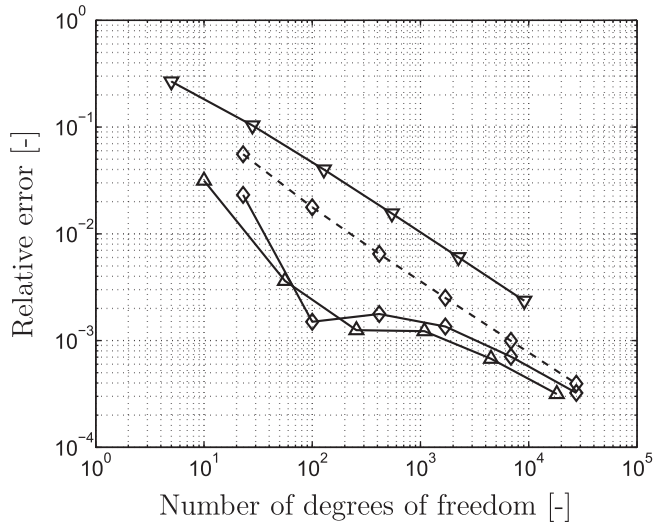


**Fig. 15.** Relative error for the lowest eigenvalue as a function of the number of degrees of freedom $N \propto 1/h^2$ for the L-shaped domain shown in Fig. 14: ($\diamond$) proposed element with $\gamma = \gamma_{\text{opt}} = 1.19$ shown by the dashed line and $\gamma = 10\gamma_{\text{opt}}$ shown by the solid line; ($\triangledown$) incomplete linear edge element; and ($\triangle$) complete linear edge element.

## 5. Conclusion

We have proposed a linear nonconforming finite element for Maxwell's equations formulated in two space dimensions. The element shape functions have degrees of freedom associated with the midpoints of the edges of the element. The tangential field at the midpoint of each edge is continuous, while the normal component is allowed to be discontinuous, yielding an approximation related to the Crouziex–Raviart element for Stokes. Our formulation features a parameter $\gamma$ that stabilizes the tangential continuity at element edges, which allows for tuning aimed at improving the accuracy of the method.

We conclude that the proposed element yields a discretization error that is proportional to the square of the mesh size for problems with smooth boundaries, which is expected since it can model linear field variations exactly. A numerical dispersion analysis on a periodic grid shows that the proposed element yields second order convergence towards the analytical dispersion relation. For the case with stabilization, we find four branches with $\omega(\boldsymbol{k}) = 0$ that correspond to modes with an

irrotational electric field that can be expressed as the gradient of a scalar potential: (i) one linear Lagrangian basis function $\phi_i$ associated with the node of the unit cell; and (ii) three edge-bubble basis functions $\phi_i\phi_j$ associated with the three edges of the unit cell (the case without stabilization yields three additional branches with $\omega(\boldsymbol{k}) = 0$). The lowest non-zero branch $\omega(\boldsymbol{k})$ corresponds to the physical dispersion relation and it shows a relative error that is proportional to $(h_T k)^2$ in the asymptotic region of convergence, where $h_T$ denotes the maximum edge length of the mesh. The remaining non-zero branches yield very large values for $\omega(\boldsymbol{k})$, which makes them easy to identify and disregard. We find that it is feasible to optimize the stabilization parameter $\gamma$ on a periodic grid of equilateral triangles in order to achieve very low errors in the dispersion relation for large regions in $\boldsymbol{k}$-space.

Eigenvalue analysis of a square shaped cavity reinforces the convergence properties found in the dispersion analysis. We emphasize that the proposed element does not suffer from spurious solutions and that it reproduces the well-resolved eigenvalues with the correct multiplicity, also for problems where the field solution is singular. Finally, we conclude that the proposed element allows for explicit time-stepping and yields accurate and robust results. These characteristic features make our element very suitable for computationally challenging electromagnetic field problems that feature complex geometry, e.g. large conformal array antennas.

## Acknowledgment

Thomas Rylander was supported in part by the Strategic Research Center CHARMANT, financed by the Swedish Foundation for Strategic Research.

## References

[1] J.C. Nédélec, Mixed finite elements in $\mathbb{R}^3$, Numer. Math. 35 (3) (1980) 315–341.
[2] J.C. Nédélec, A new family of mixed finite elements in $\mathbb{R}^3$, Numer. Math. 50 (1986) 57–81.
[3] P. Monk, Finite Element Methods for Maxwell's Equations, Oxford University Press, New York, NY, 2003.
[4] Y. Haugazeau, P. Lacoste, Condensation de la matrice masse pour les éléments finis mixtes de H(rot), C.R. Acad. Sci. Paris Ser. I 316 (1993) 509–512.
[5] P. Lacoste, La condensation de la matrice masse, ou mass-lumping, pour les éléments finis mixtes de Raviart–Thomas–Nédélec d'ordre 1, C.R. Math. Acad. Sci. Paris 339 (2004) 727–732.
[6] A. Elmkies, P. Joly, Éléments finis d'arête et condensation de masse pour les équations de Maxwell: le cas 2D, C.R. Acad. Sci. Paris t. 324 (Série I) (1997) 1287–1293.
[7] G. Cohen, Higher Order Numerical Methods for Transient Wave Equations, Springer, Berlin, 2002.
[8] K.S. Yee, Numerical solution of initial boundary value problems involving Maxwell's equations in isotropic media, IEEE Trans. Anten. Propagat. AP-14 (3) (1966) 302–307.
[9] A. Taflove, S.C. Hagness, Computational Electrodynamics: The Finite-Difference Time-Domain Method, third ed., Artech House, Boston, MA, 2005.
[10] D. Degerfeldt, T. Rylander, A brick-tetrahedron finite-element interface with stable hybrid explicit-implicit time-stepping for Maxwell's equations, J. Comput. Phys. 220 (2006) 383–393.
[11] A. Buffa, P. Houston, I. Perugia, Discontinuous Galerkin computation of the Maxwell eigenvalues on simplicial meshes, J. Comput. Appl. Math. 204 (2007) 317–333.
[12] I. Perugia, D. Schötzau, P. Monk, Stabilized interior penalty methods for the time–harmonic Maxwell equations, Comput. Meth. Appl. Mech. Eng. 191 (2002) 4675–4697.
[13] T. Warburton, M. Embree, The role of the penalty in the local discontinuous Galerkin method for Maxwell's eigenvalue problem, Comput. Meth. Appl. Mech. Eng. 195 (2006) 3205–3223.
[14] J.S. Hesthaven, T. Warburton, High-order accurate methods for time-domain electromagnetics, Comput. Model. Eng. Sci. 5 (5) (2004) 395–407.
[15] J.P. Bérenger, A perfectly matched layer for the absorption of electromagnetic waves, J. Comput. Phys. 114 (2) (1994) 185–200.
[16] J.M. Jin, The Finite Element Method in Electromagnetics, second ed., John Wiley & Sons, New York, NY, 2002.
[17] T. Rylander, J.M. Jin, Perfectly matched layer for the time domain finite element method, J. Comput. Phys. 200 (1) (2004) 238–250.
[18] T. Rylander, A. Bondeson, Stable FEM–FDTD hybrid method for Maxwell's equations, Comput. Phys. Commun. 125 (2000) 75–82.
[19] M. Crouzeix, P.A. Raviart, Conforming and nonconforming finite element methods for solving the stationary Stokes equations, RAIRO Sér. Rouge 7 (1973) 33–75.
[20] S.C. Brenner, F. Li, L.Y. Sung, A locally divergence-free nonconforming finite element method for the time-harmonic Maxwell equations, Math. Comput. 76 (2007) 573–595.
[21] S.C. Brenner, F. Li, L.Y. Sung, A locally divergence-free interior penalty method for two-dimensional curl-curl problems, SIAM J. Numer. Anal. 46 (2008) 1190–1211.
[22] S.C. Brenner, F. Li, L.Y. Sung, Nonconforming Maxwell eigensolvers, J. Sci. Comput. 40 (2009) 51–85.
[23] S.C. Brenner, J. Cui, F. Li, L.Y. Sung, A nonconforming finite element method for a two-dimensional curl–curl and grad–div problem, Numer. Math. 109 (2008) 509–533.
[24] P. Hansbo, M.G. Larson, Discontinuous Galerkin and the Crouzeix–Raviart element: application to elasticity, ESAIM: Math. Model. Numer. Anal. 37 (2003) 63–72.
[25] A. Buffa, I. Perugia, Discontinuous Galerkin approximation of the Maxwell eigenproblem, SIAM J. Numer. Anal. 44 (2006) 2198–2226.
[26] E. Burman, P. Hansbo, A stabilized non-conforming finite element method for incompressible flow, Comput. Meth. Appl. Mech. Eng. 195 (2006) 2881–2899.
[27] P. Houston, I. Perugia, A. Schneebeli, D. Schötzau, Interior penalty method for the indefinite time-harmonic maxwell equations, Numer. Math. 100 (2005) 485–518.
[28] K.D. Paulsen, D.R. Lynch, Elimination of vector parasites in finite element Maxwell solutions, IEEE Trans. Microw. Theor. Tech. 39 (3) (1991) 395–404.
[29] P.B. Monk, A comparison of three mixed methods for the time dependent Maxwell equations, SIAM J. Sci. Stat. Comput. 13 (5) (1992) 1097–1122.
[30] C. Geuzaine, B. Meys, P. Dular, W. Legros, Convergence of high order curl-conforming finite elements, IEEE Trans. Magn. 35 (3) (1999) 1442–1445.
[31] J.P. Webb, Hierarchal vector basis functions of arbitrary order for triangular and tetrahedral finite elements, IEEE Trans. Anten. Propagat. 47 (8) (1999) 1244–1253.
[32] A. Bondeson, T. Rylander, P. Ingelström, Computational Electromagnetics, Springer, Berlin, 2005.